J. Fluid Mech. (2009), *vol.* 641, *pp.* 497–507.
doi:10.1017/S0022112009991947

Expanding the Q–R space to three dimensions

BEAT LÜTHI[1,2]†,
MARKUS HOLZNER[1,2] AND ARKADY TSINOBER[1,3]

[1]International Collaboration for Turbulence Research

[2]Institute of Environmental Engineering, ETH Zurich, Wolfgang-Pauli-Strasse 15, 8093 Zurich, Switzerland

[3]School of Mechanical Engineering, Faculty of Engineering, Tel Aviv University, Tel Aviv 69978, Israel

(Received 31 May 2009; revised 3 September 2009; accepted 3 September 2009)

The two-dimensional space spanned by the velocity gradient invariants Q and R is expanded to three dimensions by the decomposition of R into its strain production $-1/3 s_{ij}s_{jk}s_{ki}$ and enstrophy production $1/4\omega_i\omega_j s_{ij}$ terms. The $\{Q;R\}$ space is a planar projection of the new three-dimensional representation. In the $\{Q;-sss;\omega\omega s\}$ space the Lagrangian evolution of the velocity gradient tensor A_{ij} is studied via conditional mean trajectories (CMTs) as introduced by Martín *et al.* (*Phys. Fluids*, vol. 10, 1998, p. 2012). From an analysis of a numerical data set for isotropic turbulence of $Re_\lambda \sim 434$, taken from the Johns Hopkins University (JHU) turbulence database, we observe a pronounced cyclic evolution that is almost perpendicular to the Q–R plane. The relatively weak cyclic evolution in the Q–R space is thus only a projection of a much stronger cycle in the $\{Q;-sss;\omega\omega s\}$ space. Further, we find that the restricted Euler (RE) dynamics are primarily counteracted by the deviatoric non-local part of the pressure Hessian and not by the viscous term. The contribution of the Laplacian of A_{ij}, on the other hand, seems the main responsible for intermittently alternating between low and high intensity A_{ij} states.

Key words: dynamics, isotropic, theory

1. Introduction

The understanding of the small-scale structure of turbulence has been at the core of turbulence research for a few decades now (see, e.g. Tennekes & Lumley 1972; Frisch 1995; Sreenivasan & Antonia 1997; Tsinober 2001). It was natural to investigate the properties of the velocity gradient tensor $A_{ij} = \partial u_i/\partial x_j$ (e.g. Ashurst, Kerstein & Kerr 1987; Lund & Rogers 1994; Soria *et al.* 1994; Galanti & Tsinober 2000; Kholmyansky, Tsinober & Yorish 2001; Lüthi, Tsinober & Kinzelbach 2005). Well known important properties of A_{ij} are the predominant alignment of vorticity $\boldsymbol{\omega}$ with the intermediate eigenvector $\boldsymbol{\lambda}_2$ of the rate of strain tensor $s_{ij} = 1/2(A_{ij} + A_{ji})$ and the positiveness of the mean of the corresponding eigenvalue Λ_2. The evolution equations for enstrophy ω^2 and strain s^2 read

$$\frac{\mathrm{D}}{\mathrm{D}t}\frac{\omega^2}{2} = \omega_i\omega_j s_{ij} + \nu\omega_i\nabla^2\omega_i, \tag{1.1}$$

$$\frac{\mathrm{D}}{\mathrm{D}t}\frac{s^2}{2} = -s_{ij}s_{jk}s_{ki} - \frac{1}{4}\omega_i\omega_j s_{ij} - s_{ij}\frac{\partial^2 p}{\partial x_i \partial x_j} + \nu s_{ij}\nabla^2 s_{ij}. \tag{1.2}$$

† Email address for correspondence: luethi@ifu.baug.ethz.ch

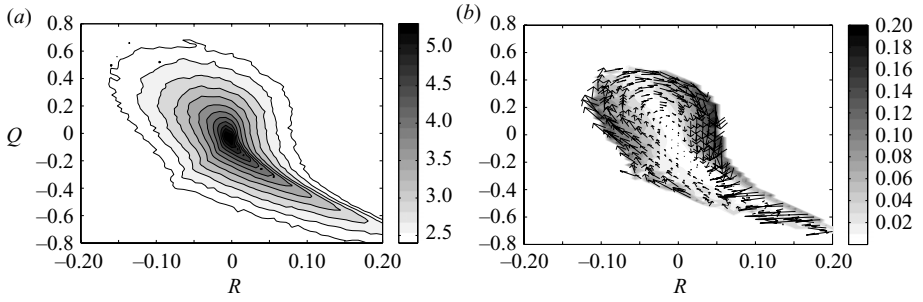

FIGURE 1. (*a*) Joint p.d.f. of A_{ij} events in the invariant space $\{Q;R\}$, plotted in $\log_{10}$ spaced contours. (*b*) Vector field and magnitude of the non-dimensional conditional mean rate of change, $\overline{\boldsymbol{v}}_{Q,R}$, in the $\{Q;R\}$ space.

Equations (1.1) and (1.2) indicate that along with ω^2 and s^2, the third moments, enstrophy and strain production, $\omega_i\omega_j s_{ij}$ and $s_{ij}s_{jk}s_{ki}$, are among the key quantities of turbulence dynamics. They are responsible for the self-amplifying nature of A_{ij}, which is believed to be a universal feature, as is discussed in Tsinober (2001). Another important relation is the so-called Tennekes and Lumley balance (Tennekes & Lumley 1972, p. 91) for statistically stationary turbulence $\langle\omega_i\omega_j s_{ij}\rangle = -\langle\nu\omega_i\nabla^2\omega_i\rangle$. It states that, at whatever high Reynolds number, the viscous and production terms of enstrophy are of equal importance. It is notable that even at low Reynolds number the integrals over the flow domain of the enstrophy production and of its viscous destruction are approximately balanced at any time moment, $\int\omega_i\omega_j s_{ij}\mathrm{d}V \approx -\nu\int\omega_i\nabla^2\omega_i\mathrm{d}V$, as reported in Tsinober (2001).

It has proven to be a useful way to study some of the local flow properties in the so called Q–R plane (e.g. Cantwell 1992; Martín, Dopazo & Valiño 1998; Ooi *et al.* 1999; Chertkov, Pumir & Shraiman 1999; Biferale *et al.* 2007; Chevillard *et al.* 2008). Q is the second invariant, $Q = 1/4(\omega^2 - 2s^2)$, of the velocity gradient tensor A_{ij} and R is its third invariant, $R = -1/3s_{ij}s_{jk}s_{ki} - 1/4\omega_i\omega_j s_{ij}$. In joint p.d.f. plots of Q versus R a qualitatively identical 'tear drop' shape (see figure 1*a*) for different kinds of turbulent flows was found by a number of investigators. Chacín & Cantwell (2000) argue that the shape is a universal characteristic of the small-scale motions of turbulence. This statement is corroborated by a compilation of Q–R plots of different flows (Tsinober 2001) and velocity gradient measurements at $Re_\lambda = 6600$ (see Gulitski *et al.* 2007). The most characteristic feature is that in strain dominated regions the strain production term, $-s_{ij}s_{jk}s_{ki}$, is dominant over $\omega_i\omega_j s_{ij}$, resulting in the so-called Vieillefosse tail, (see Vieillefosse 1982).

Neglecting the non-local influence of pressure and viscosity H_{ij}, Cantwell (1992) derived the so-called restricted Euler (RE) solution for the evolution of A_{ij} as $\mathrm{d}Q/\mathrm{d}t = -3R$ and $\mathrm{d}R/\mathrm{d}t = -2/3Q^2$. In Chacín & Cantwell (2000) the analysis is extended to studying and modelling the term H_{ij}. The same authors employed the Q–R framework to investigate flow structures of turbulent boundary layers (Chacín & Cantwell 2000). A central finding was that the discriminant, $D = 27/4\cdot R^2 + Q^3$, of A_{ij} separates sweeps and strong dissipative events $D < 0$ from ejections $D > 0$. They concluded that additional insight into turbulent motions can be gained by studying the Lagrangian evolution of A_{ij} in the Q–R plane. Martín *et al.* (1998) and Ooi *et al.* (1999) identified a mean clockwise evolution of trajectories in the Q–R plane. Several studies aimed at comprehending and modelling this mean evolution (e.g. Chertkov *et al.* 1999; Jeong & Girimaji 2003; Chevillard *et al.* 2008). The 'fluid deformation'

Grid	Δt	$\varepsilon = 2\nu s_{ij}s_{ij}$	ν	$\tau_\eta = \left(\frac{\nu}{\varepsilon}\right)^{1/2}$	L	$\eta = \left(\frac{\nu^3}{\varepsilon}\right)^{1/4}$	$Re_\lambda = \sqrt{15}\left(\frac{L}{\eta}\right)^{2/3}$
1024^3	2×10^{-4}	0.0928	1.85×10^{-4}	0.0446	3.4	0.00287	434

TABLE 1. Parameters of the numerical JHU simulation.

closure for the deviatoric part of the pressure Hessian H_{ij}^P introduced by Chevillard *et al.* (2008) works well in regions with $D < 0$; however, in regions where $D > 0$ some features are not accurately reproduced. Generally, when projected onto the Q–R plane, the role of H_{ij}^P remains somewhat unclear, for example, in the region where $D > 0$ and $R > 0$ the averaged influence of H_{ij}^P is almost negligible.

In the present study the $\{Q; R\}$ space is expanded to three dimensions, $\{Q; -sss; \omega\omega s\}$. This new representation allows to shed more light on the dynamics of the velocity gradient tensor A_{ij}. Among other things, the role of H_{ij}^P becomes much clearer. This paper is organized as follows. In § 2 the details of the numerical JHU data are outlined. In § 3 Q–R dynamics together with a definition for its variance of magnitude and direction are introduced. The evolution of A_{ij} in $\{Q; -sss; \omega\omega s\}$ space, with special attention to the deviatoric part of the pressure Hessian is presented in § 4, which is followed by summary and conclusions in § 5.

2. JHU data

For our analysis we have used the JHU turbulence database that is developed as an open resource by the Johns Hopkins University (see Li *et al.* 2008). The data is from a direct numerical simulation of forced isotropic turbulence on a 1024^3 periodic grid, using a pseudospectral parallel code. The Taylor Reynolds number is $Re_\lambda = 434$. Time integration of the viscous term is done analytically using an integrating factor. The other terms are integrated using a second-order Adams–Bashforth scheme and the nonlinear term is written in vorticity form, following Cao & Chen (1999). The simulation is de-aliased using phase-shift and a $2\sqrt{2}/3$ truncation (see Patterson & Orszag 1971). Energy is injected by keeping constant the total energy in modes such that their wavenumber magnitude is less or equal to 2. After the simulation has reached a statistical stationary state, 1024 frames of data, which includes the three components of the velocity vector and the pressure, are generated and ingested into the database. The duration of the stored data is about one large-eddy turnover time. For our analysis we have released 8×10^6 particles into the flow at $t = 0$ and integrated their position in time using the Euler method with a time step of $\delta t = 1/22\tau_\eta$. At every new position the information of velocity, pressure Hessian and the Laplacian of A_{ij} was stored. A summary of the flow parameters is given in table 1.

3. Q–R dynamics and variance of evolution

Following Martín *et al.* (1998), we calculate the Lagrangian non-dimensional instantaneous rates of change $\boldsymbol{v}_{Q,R}$ as $\{\dot{Q} = DQ/Dt \cdot \tau_\eta | Q, R; \dot{R} = DR/Dt \cdot \tau_\eta | Q, R\}$ as functions of the velocity gradient invariant variables Q and R, and the corresponding conditional mean rates of change $\overline{\boldsymbol{v}}_{Q,R}$ as $\{\langle \dot{Q} | Q, R\rangle; \langle \dot{R} | Q, R\rangle\}$. Note that if $\langle \dot{Q} | Q, R\rangle$ and $\langle \dot{R} | Q, R\rangle$ were multiplied by the joint probability $P(Q, R)$ it would be identical to the probability current $\mathscr{W}$ as used, for example, in Chevillard *et al.* (2008). In all our results Q and R have been normalized with τ_η^2 and τ_η^3, respectively. $\dot{Q}$ and $\dot{R}$ can

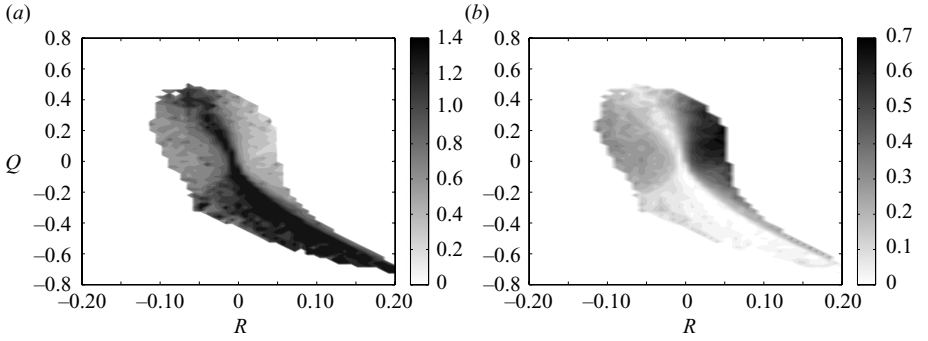

FIGURE 2. (*a*) Q–R conditioned contour plots with $\log_{10}$ spacing of the relative variance $\widehat{\sigma} = \sigma_v/\|\overline{\boldsymbol{v}}_{Q,R}\|$. (*b*) Q–R conditioned contour plots of $\|\langle\cos(\overline{\boldsymbol{v}}_{Q,R}, \boldsymbol{v}_{Q,R})\rangle\|$.

be looked at as components of a velocity vector $\boldsymbol{v}_{Q,R}$ of the state of A_{ij} in the Q–R space. In figure 1(*b*) we plot the vector field and the contours of the magnitude of $\overline{\boldsymbol{v}}_{Q,R}$. From, for example, Martín *et al.* (1998) it is known that the conditional mean trajectories of $\boldsymbol{v}_{Q,R}$ circle in a clockwise direction around the origin. What is perhaps less well known and demonstrated here, is that $\|\overline{\boldsymbol{v}}_{Q,R}\|$ tends to very small values along the centreline of the 'tear drop' shape, which for $Q < 0$ regions coincides with the so-called Vieillefosse tail (Vieillefosse 1982).

By defining a mean and a fluctuating part as $\boldsymbol{v}_{Q,R} = \overline{\boldsymbol{v}}_{Q,R} + \boldsymbol{v}'_{Q,R}$, the variance of $\boldsymbol{v}_{Q,R}$ is $\sigma_v^2 = \langle(\boldsymbol{v}_{Q,R} - \overline{\boldsymbol{v}}_{Q,R})^2\rangle$. In figure 2(*a*) logarithmically spaced contours are shown for $\widehat{\sigma} = \sigma_v/\|\overline{\boldsymbol{v}}_{Q,R}\|$. We see that only in the relatively high speed regions, $\widehat{\sigma}$ drops to small values where $\|\overline{\boldsymbol{v}}_{Q,R}\|$ and $\|\boldsymbol{v}_{Q,R}\|$ are of similar order. Around the Vieillefosse tail however, $\|\boldsymbol{v}_{Q,R}\|$ is typically over an order of magnitude larger than $\|\overline{\boldsymbol{v}}_{Q,R}\|$. The same trend becomes apparent if we look at the low values of the mean cosine of the angle between $\overline{\boldsymbol{v}}_{Q,R}$ and $\boldsymbol{v}_{Q,R}$, shown in figure 2(*b*). On the one hand, it is not surprising that the cosine is far from unity, as it is clear that $\boldsymbol{v}_{Q,R}$ must have significant components normal to the iso-probability contours of the joint p.d.f. of Q and R. Otherwise a fluid parcel with low gradients could not reach strong enstrophy or strain states as intermittently as it occurs in turbulence. We find that this alternation between low and high intensity states is quite intensive, since even the strongest mean alignment in the quadrant $Q > 0$ and $R > 0$ never exceeds an angle of 45° and is very close to random alignment around the Vieillefosse tail.

4. Evolution in $\{Q; -sss; \omega\omega s\}$ space

In this section the $\{Q; R\}$ space is expanded to three dimensions so that the influence of strain and enstrophy production terms $-s_{ij}s_{jk}s_{ki}$ and $\omega_i\omega_j s_{ij}$ can be studied separately. For the analysis of the $\{Q; -sss; \omega\omega s\}$ space a total of $106\times40\times40$ bins are used in a domain $\{[-0.8\boldsymbol{e}_1, 0.8\boldsymbol{e}_1], [-0.3\boldsymbol{e}_2, 0.3\boldsymbol{e}_2], [-0.3\boldsymbol{e}_3, 0.3\boldsymbol{e}_3]\}$. The norms of the $\boldsymbol{e}_i$ triplet in the three directions are equivalent to

$$\left.\begin{aligned}\|\boldsymbol{e}_1\| &= 1/4(\omega^2 - 2s^2),\\ \|\boldsymbol{e}_2\| &= -1/3\sqrt{2}s_{ij}s_{jk}s_{ki},\\ \|\boldsymbol{e}_3\| &= 1/4\sqrt{2}\omega_i\omega_j s_{ij}.\end{aligned}\right\} \tag{4.1}$$

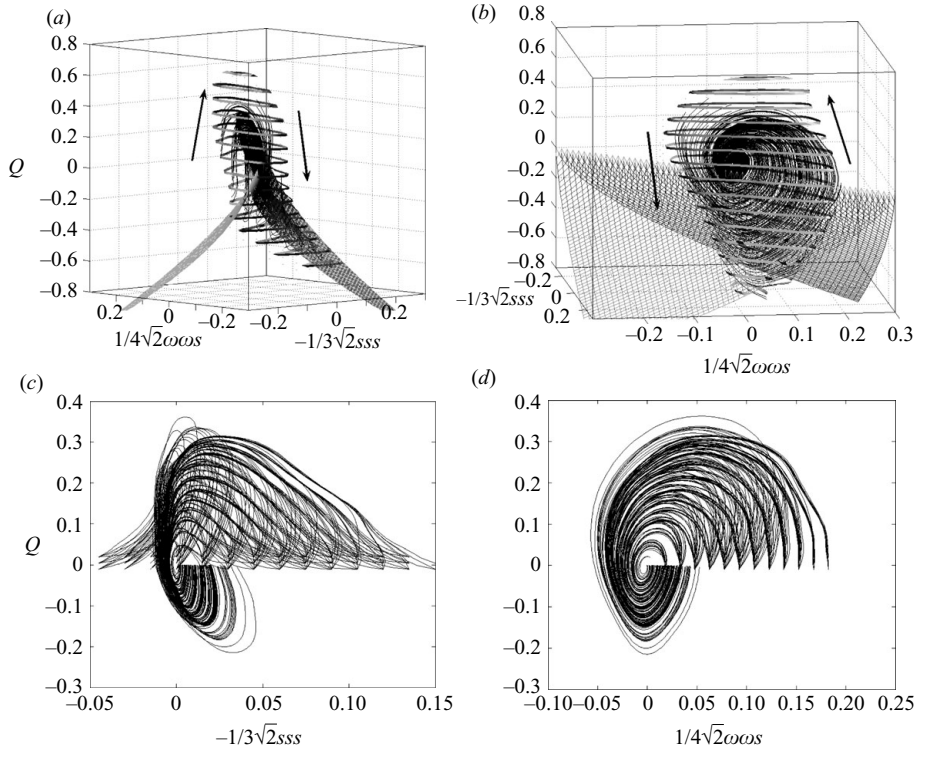

FIGURE 3. Conditional mean trajectories (CMTs) of the evolution of A_{ij} in the $\{Q; -sss; \omega\omega s\}$ space are shown for two different views inside $V_{95\,\%}$ represented by ribbons, with the arrows indicating the direction of the CMTs. The surface with the discriminant $D = 27/4 \cdot R^2 + Q^3 = 0$ is shown as a wire mesh. The view point of (*a*) is chosen such that the envelope of the ribbons resemble the 'tear drop' shape and the clockwise cyclic evolution, known from the two-dimensional Q–R representation. The three-dimensional view (*b*) reveals the cyclic evolution more clearly. All CMTs starting at the centre of a bin inside $V_{95\,\%}$ from the $Q = 0$ plane with $\dot{Q} > 0$ are plotted (*c*) in the $\{-1/3\sqrt{2}sss; Q\}$ plane and (*d*) in the $\{1/4\sqrt{2}\omega\omega s; Q\}$ plane, for one complete cycle.

The pre-factors $\sqrt{2}$ for the production terms are used so that for the planar projection onto the $\{Q; R\}$ space we have $\boldsymbol{e}_2 - \boldsymbol{e}_3 = \boldsymbol{e}_R$. This domain spans five times the averages of enstrophy (strain) and enstrophy (strain) production. Each bin that contains more than five entries is used to define a joint probability volume. We find that for our data 95 % of all events fall into the volume represented by ribbons in figure 3(*a*, *b*) and it is henceforth referred to as $V_{95\,\%}$. Similar to $\{Q; R\}$ space (see Martín *et al.* 1998) we define the conditional mean rates of change for the $\{Q; -sss; \omega\omega s\}$ space as

$$\left.\begin{aligned} \overline{\boldsymbol{v}}_Q &= \left\langle \frac{DQ}{Dt} \cdot \tau_\eta^3 \mid Q, -1/3\sqrt{2}sss, 1/4\sqrt{2}\omega\omega s \right\rangle \\ \overline{\boldsymbol{v}}_{sss} &= \left\langle \frac{D(-1/3\sqrt{2}s_{ij}s_{jk}s_{ki})}{Dt} \cdot \tau_\eta^4 \mid Q, -1/3\sqrt{2}sss, 1/4\sqrt{2}\omega\omega s \right\rangle \\ \overline{\boldsymbol{v}}_{\omega\omega s} &= \left\langle \frac{D(1/4\sqrt{2}\omega_i\omega_j s_{ij})}{Dt} \cdot \tau_\eta^4 \mid Q, -1/3\sqrt{2}sss, 1/4\sqrt{2}\omega\omega s \right\rangle . \end{aligned}\right\} \tag{4.2}$$

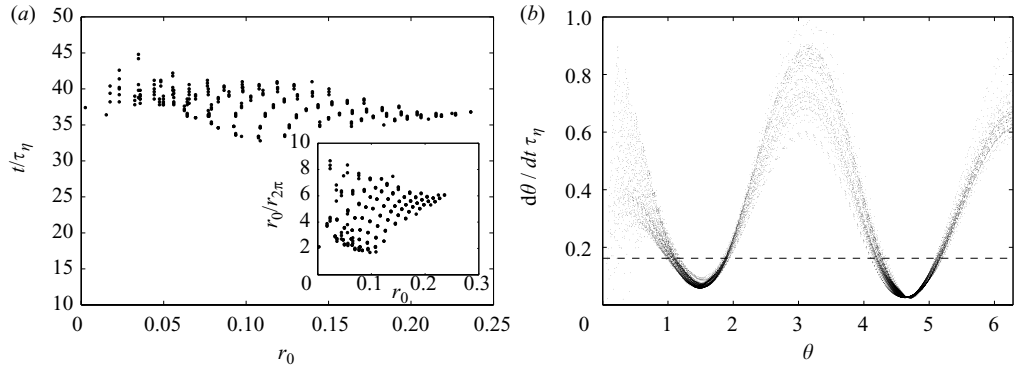

FIGURE 4. (a) For each CMT shown in figure 3(c, d) the duration of one revolution is measured and plotted versus its initial distance from the origin r_0. The inset shows the ratio, $r_0/r_{2\pi}$, between the distances from to origin before and after one complete cycle. (b) For the same CMTs the angular velocity $\mathrm{d}\theta/\mathrm{d}t \cdot \tau_\eta$ is plotted over the angle θ of the $\{1/4\sqrt{2}\omega\omega s; Q\}$ state. The dashed line is at $\langle \mathrm{d}\theta/\mathrm{d}t \cdot \tau_\eta \rangle = 0.16$.

Analogously to the two-dimensional case, (4.2) represents the three components of a velocity vector $\boldsymbol{v}$ of A_{ij} in the $\{Q; -sss; \omega\omega s\}$ space. Like for $\{Q; R\}$, Q and the production terms are normalized with τ_η^2 and τ_η^3, respectively. To illustrate that the Q–R plane is a projection of the $\{Q; -sss; \omega\omega s\}$ space we show in figure 3(a) the evolution of conditional mean trajectories (CMTs) starting from the centre of each bin within $V_{95\,\%}$ from a view point approximately perpendicular to the Q–R plane, i.e. $\{Q \cdot \boldsymbol{e}_1; [-1/3\sqrt{2}sss \cdot \boldsymbol{e}_2 - 1/4\sqrt{2}\omega\omega s \cdot \boldsymbol{e}_3]\}$. The surface of $D = 0$, with the discriminant $D = 27/4 \cdot R^2 + Q^3$, is rendered as a wire mesh. From this view point the well known clockwise evolution is evident in the enstrophy dominated regions where $Q > 0$, while around the Vieillefosse tail the evolution is less clear. However, if the view point is moved such that it is facing almost the Q–$\omega\omega s$ plane (figure 3b), our first main result becomes much clearer: There is a pronounced anticlockwise cyclic evolution, with a rotation axis that is almost perpendicular to the Q–R plane. This non-trivial cyclic evolution is one of the manifestations of the time irreversibility of turbulent flows, as reflected by other manifestations, such as positive net enstrophy and strain production and the 4/5 Kolmogorov law. To better illustrate the characteristics of the CMTs, we show in figure 3(c, d) selected CMTs that start from the $Q = 0$ plane with $\dot{Q} > 0$ at the centre of each bin inside $V_{95\,\%}$. The CMTs are integrated over one revolution until they cross again the $Q = 0$ plane. Figure 3(c) shows how during vortex compression ($\omega\omega s < 0$ and $-sss \sim 0$) all CMTs are attracted towards a very narrow region, before diverging again slightly in the strain dominated region ($Q < 0$). Figure 3(d) reveals how the CMTs spiral towards the origin. Summarizing, a typical cycle for all CMTs starts with enstrophy production ($\omega\omega s > 0$) often associated with strain production ($-sss > 0$) leading to enstrophy dominated regions ($Q > 0$). This is followed by vortex compression ($\omega\omega s < 0$) while the CMTs reach strain dominated regions ($Q < 0$).

To quantify the cyclic evolution of A_{ij} figure 4(a) reveals that complete revolutions of all CMTs shown in figure 3(c,d) have a duration of about $40\tau_\eta$, regardless of r_0, the initial distance of a CMT from the origin. During one cycle the distance r roughly diminishes by a factor of 5, as seen in the inset of the same figure. The angular velocities, $\mathrm{d}\theta/\mathrm{d}t \cdot \tau_\eta$, of the CMTs are measured and plotted over the angle θ, with $\tan(\theta) = Q/(1/4\sqrt{2}\omega\omega s)$ (figure 4b). On average $\mathrm{d}\theta/\mathrm{d}t \cdot \tau_\eta = 0.16$, which results in a

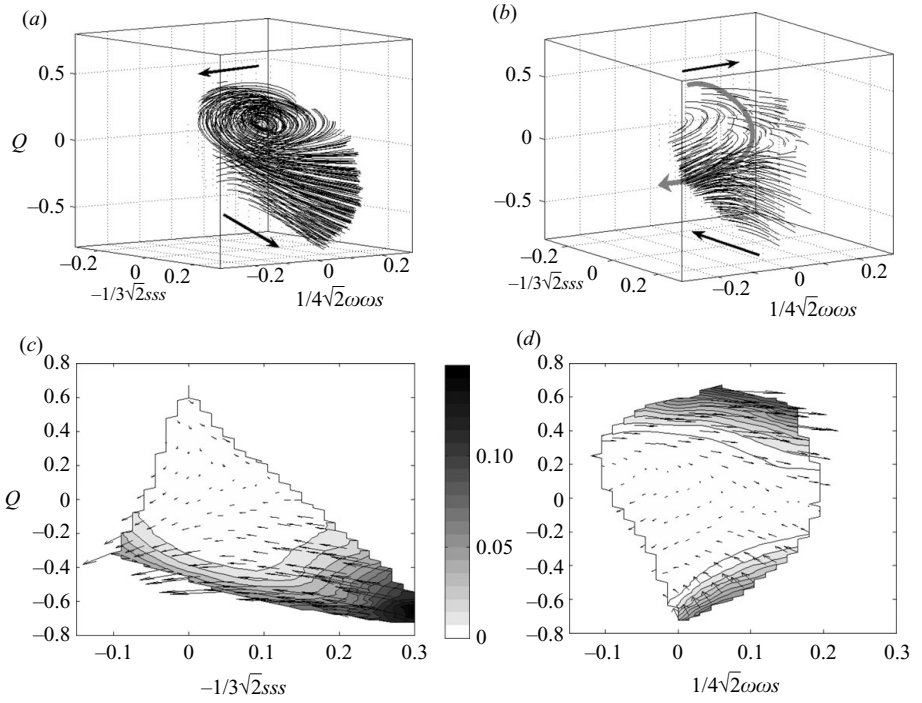

FIGURE 5. (*a*) CMTs of the RE contribution to the evolution of A_{ij} inside the $V_{95\,\%}$ volume in the $\{Q;-sss;\omega\omega s\}$ space. (*b*) CMTs of the H_{ij}^{P} contribution to the evolution of A_{ij} inside the $V_{95\,\%}$ volume. The arrows are indicating the direction of the CMTs. (*c*) Projection of the $\overline{\boldsymbol{v}}^{P}$ field onto the $\{-1/3\sqrt{2}sss;Q\}$ plane with iso-contours for its magnitude. (*d*) Same as (*c*) but projection onto the $\{1/4\sqrt{2}\omega\omega s;Q\}$ plane.

cycle duration of $2\pi/0.16 \simeq 39\tau_\eta$ that is of the order of the integral time $T_L \simeq 60\tau_\eta$. Without access to A_{ij} dynamics at significantly higher Reynolds number it is not clear how the cycle duration is determined by T_L and τ_η, i.e. how it is affected by direct and bidirectional coupling between small and large scales. The good collapse of all curves at $\theta = \pi/2$ and $3\pi/2$, where the CMTs reach their extreme values of positive and negative Q, is noteworthy.

Taking the gradient of the Navier–Stokes equation one obtains

$$\frac{DA_{ij}}{Dt} = -A_{ik}A_{kj} - \frac{\partial^2 p}{\partial x_i \partial x_j} + \nu \frac{\partial^2 A_{ij}}{\partial x_k \partial x_k}. \tag{4.3}$$

Using the incompressibility condition $A_{ii} = 0$, the pressure is given by

$$A_{ik}A_{ki} = -\frac{\partial^2 p}{\partial x_i \partial x_i}. \tag{4.4}$$

Subtracting (4.4) from (4.3) with the condition that the trace of the pressure term be zero produces

$$\frac{DA_{ij}}{Dt} = -A_{ik}A_{kj} + A_{km}A_{mk}\frac{\delta_{ij}}{3} - \frac{\partial^2 p}{\partial x_i \partial x_j} + \frac{\partial^2 p}{\partial x_i \partial x_i}\frac{\delta_{ij}}{3} + \nu \frac{\partial^2 A_{ij}}{\partial x_k \partial x_k}. \tag{4.5}$$

The first two terms of the right-hand side of (4.5) lead to the well-known RE solution (Cantwell 1992) in the $\{Q;R\}$ space and the corresponding CMTs for $\boldsymbol{v}^{RE}$ in

three-dimensional space are shown in figure 5(*a*). The main characteristic of the RE trajectories is that they are not doomed to spiral and converge towards the origin, but that they escape and leave the volume at high strain and enstrophy production rates. As an interesting additional feature we observe that any CMT starting at $D > 0$ first makes a looping, peaking at high enstrophy values, before reaching high production rates. We observed that adding the viscous term of (4.5) does hardly change the qualitative behaviour of the CMTs. The field $\overline{\boldsymbol{v}}^{\nu}$ of $\nu\nabla^2 A_{ij}$ is relatively weak and is mainly pointing towards the origin (Chevillard *et al.* 2008 and own observations not shown herein).

Chevillard *et al.* (2008) studied the role of the deviatoric part of the pressure Hessian H_{ij}^P and reported two main features. First, H_{ij}^P is counteracting the effect induced by the RE term. Second, in the quadrant above the right Vieillefosse tail the directions of the CMTs are uncertain due to negligible magnitudes of $\overline{\boldsymbol{v}}_{R,Q}^p$. The action of the deviatoric part of the pressure Hessian in the $\{Q; -sss; \omega\omega s\}$ space is shown in figure 5(*b*). As expected, also in the three-dimensional representation the action of H_{ij}^P is counteracting the RE contribution. Generally, the magnitude of $\overline{\boldsymbol{v}}^p$ increases with increasing $\|Q\|$ (figure 5*c*,*d*) and is maximal in high strain regions, where H_{ij}^P counteracts strain production, as indicated by the lower arrow in figure 5(*b*) and as can be clearly seen in the projection of the $\overline{\boldsymbol{v}}^P$ field onto the $\{-1/3\sqrt{2}sss; Q\}$ plane, rendered in figure 5(*c*). In high enstrophy regions H_{ij}^P enhances enstrophy production and thereby counteracts the contribution of RE, figure 5(*d*). Again, adding to H_{ij}^P the viscous term does not change the qualitative picture. This comprises our second main result: For the dynamics of A_{ij} the deviatoric *non-local* part of the pressure Hessian and not the viscous term is predominantly counteracting the RE dynamics. In addition, we note that unlike the trajectories in $\{Q; R\}$ space, the CMTs of $\overline{\boldsymbol{v}}^p$ are quite ordered in three dimensions. The main features are that from the alignment with the $\boldsymbol{e}_3$ ($\omega\omega s$) axis at high Q (figure 5*d*) the CMTs tend towards negative Q while turning 270° at very low magnitudes of $\overline{\boldsymbol{v}}^p$ (see grey arrow in figure 5*b*) to align with the $-\boldsymbol{e}_2$ (sss) axis moving towards strain destruction (figure 5*c*). The combined influence of RE and H_{ij}^P, the evolution of the inviscid CMTs, is shown in figure 6(*a*) and reveals a clear pattern. In contrast to the RE dynamics the cyclic evolution is now present, but the CMTs are spiralling away from the origin. Especially at high production rates of either strain or enstrophy the CMTs leave $V_{95\,\%}$ more or less at a normal angle. In $Q > 0$ regions H_{ij}^P attenuates a too strongly converging spiralling motion of RE, while in $Q < 0$ regions H_{ij}^P fully counteracts the RE field.

Finally, we investigate in more detail the variance $\widehat{\sigma}^2$. We remind that it has to be the variance that shuffles among low- and high-intensity A_{ij} events, as the CMTs themselves simply spiral towards low values of Q, sss and $\omega\omega s$. In particular, we ask whether the main contribution to $\widehat{\sigma}^2$ stems from H_{ij}^P or from $\nu\nabla^2 A_{ij}$. Because during our analysis we observed that the $\|\langle\cos(\overline{\boldsymbol{v}}, \boldsymbol{v})\rangle\|$ and the variance $\widehat{\sigma}$ commute very closely, in figure 6(*b–d*) we show for this purpose the contours of averaged conditioned cosines projected onto the $\{\omega\omega s; Q\}$ plane. In figure 6(*b*) the inviscid case is shown. In regions with $\|Q\| > 0.2$ the values are typically above 0.7 and are approaching unity where $\overline{\boldsymbol{v}}^P$ is highest. Since the variance of the RE term is zero by definition, we conclude that in those regions the influence of H_{ij}^P leads only to a relatively small variance. If the evolution of the non-local H_{ij}^P term has a vanishing variance then closures that are based only on the position in the $\{Q; -sss; \omega\omega s\}$ space should be possible. Contrarily, the viscous term that is rendered in figure 6(*c*) is fluctuating more intensively. The average alignment between $\overline{\boldsymbol{v}}$ and $\boldsymbol{v}$ never exceeds

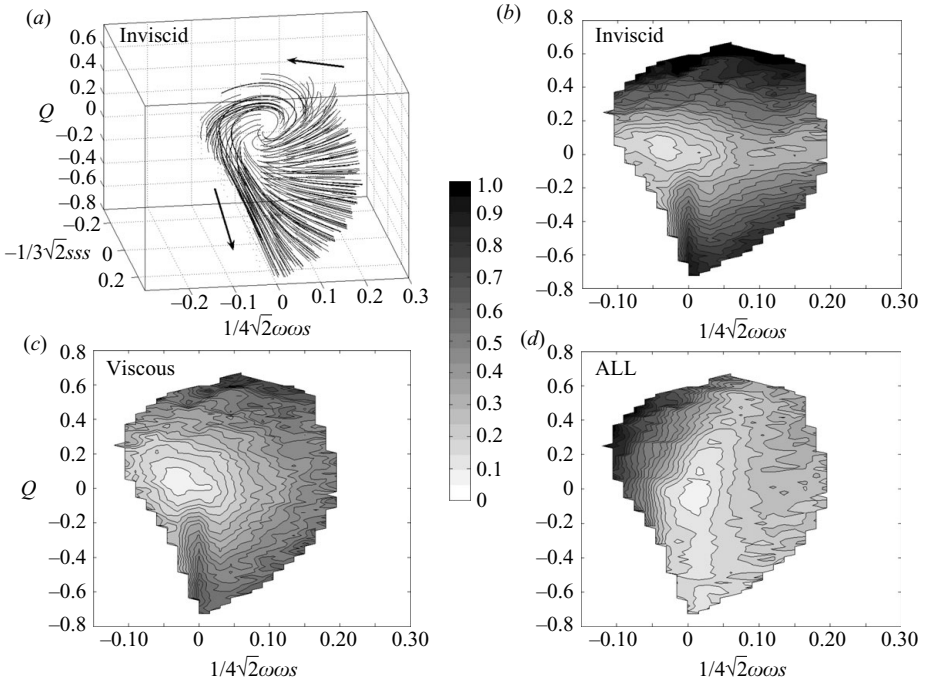

FIGURE 6. (a) Spiralling CMTs, arrows indicating the direction, of the inviscid contribution to the evolution of A_{ij} inside the $V_{95\,\%}$ volume. Contours in the $\{1/4\sqrt{2}\omega\omega s\,;\,Q\}$ plane of conditioned average cosines between the fields of mean $\overline{\boldsymbol{v}}$ and instantaneous $\boldsymbol{v}$ evolution of A_{ij} is shown for the inviscid field in (*b*), the viscous field in (*c*) and for the total field in (*d*).

45°. From this we conclude, as a third result, that the viscous term is more important than H_{ij}^{P} for alternating between low and high intensity A_{ij} events. The combined outcome for $\|\langle\cos(\overline{\boldsymbol{v}}, \boldsymbol{v})\rangle\|$ of all terms of (4.5) is shown in figure 6(*d*). Except for vortex compressing regions, where $\omega_i\omega_j s_{ij} < 0$ and $\dot{Q} < 0$ and which occupy about one third of the fluid flow volume, the alignment between $\boldsymbol{v}$ and $\overline{\boldsymbol{v}}$ is quite weak, for example, a typical angle is in the range of 10°–30°. However, as compared to the alignment of $\boldsymbol{v}_{Q,R}$–$\overline{\boldsymbol{v}}_{Q,R}$ in the $\{Q\,;R\}$ space shown in figure 2(*b*) the alignment is typically stronger.

5. Summary and conclusion

To improve fundamental understanding of the dynamics of the velocity gradient tensor A_{ij} we have expanded the two-dimensional $\{Q\,;R\}$ space to a three-dimensional $\{Q\,;-sss\,;\omega\omega s\}$ space. Analysing a numerical data set of isotropic turbulence at $Re_\lambda \sim 434$, provided by JHU turbulence database, we demonstrate that in the three-dimensional space there exists a strong cyclic evolution of the A_{ij} state. The cycle is oriented almost perpendicular to the Q–R plane and successively encounters high enstrophy/strain production events, enstrophy dominated regions, vortex compression events and strain dominated regions. The duration for one complete cycle is about $40\tau_\eta \sim O(T_L)$. Future investigations at higher Re number will show how this is affected by bi-directional coupling of small and large scales, which is the main and outstanding manifestation of non-locality (see Tsinober 2001).

Looking separately at the influences of the RE, the deviatoric part of the pressure Hessian H_{ij}^P and the viscous term $\nu\nabla^2 A_{ij}$, two additional observations can be made. First, we find that it is primarily the term H_{ij}^P that is responsible for counteracting the RE dynamics. This is not in conflict with Tsinober, Ortenberg & Shtilman (1999), who find that in regions of high strain the pressure Hessian even enhances the growth of stretching. The difference to $\partial^2 p/(\partial x_i \partial x_j)$ is that H_{ij}^P is deviatoric. Closer analysis showed that the non-local part of the pressure Hessian counteracts RE dynamics, while the local part enhances it. In future work this will be investigated in more detail.

Second, it appears that the viscous term plays the leading role for the variance of the A_{ij} evolution. We note that without such a variance, low and high intensity A_{ij} events would not be alternating as quickly as it is observed in turbulent flows, because then any A_{ij} state could evolve only along its CMTs, which are spiralling slowly towards low gradient events. The active behaviour of the viscous term reflects that it is not just a simple damping term for the inviscid dynamics of A_{ij}, i.e. that it is more active than usually thought.

We conclude by observing that the non-locality plays a crucial role for the evolution of the velocity gradients. This comprises a fundamental challenge for any closure based on local and Lagrangian history information and generally for a more complete comprehension of the A_{ij} dynamics. Our results indicate that closures for H_{ij}^P that are linked to the position in the $\{Q; -sss, \omega\omega s\}$ space should be possible. As a benchmark we propose the strong qualitative property that $\overline{\boldsymbol{v}}^P$ is aligned with $\boldsymbol{e}_3$, along $\omega\omega s$, for $Q > 0$ and with $-\boldsymbol{e}_2$, along sss, for $Q < 0$.

REFERENCES

Ashurst, W., Kerstein, A. & Kerr, R. 1987 Alignment of vorticity and scalar gradient with strain rate in simulated Navier–Stokes turbulence. *Phys. Fluids* **30** (8) 2343–2353.

Biferale, L., Chevillard, L., Meneveau, C. & Toschi, F. 2007 Multiscale model of gradient evolution in turbulent flows. *Phys. Rev. Lett.* **98** 214501.

Cantwell, B. 1992 Exact solution of a restricted euler equation for the velocity-gradient tensor. *Phys. Fluids* **4** (4) 782–793.

Cao, N. & Chen, S. 1999 Statistics and structures of pressure in isotropic turbulence. *Phys. Fluids* **14** 2538–2541.

Chacín, J. M. & Cantwell, B. J. 2000 Dynamics of a low Reynolds number turbulent boundary layer. *J. Fluid Mech.* **404** 87–115.

Chertkov, M., Pumir, A. & Shraiman, B. I. 1999 Lagrangian tetrad dynamics and the phenomenology of turbulence. *Phys. Fluids* **11** (8) 2394–2410.

Chevillard, L., Meneveau, C., Biferale, L. & Toschi, F. 2008 Modeling the pressure Hessian and viscous Laplacian in turbulence: comparisons with direct numerical simulation and implications on velocity gradient dynamics. *Phys. Fluids* **20** 101504.

Frisch, U. 1995 *Turbulence: The Legacy of A. N. Kolmogorov*. Cambridge University Press.

Galanti, B. & Tsinober, A. 2000 Self-amplification of the field of velocity derivatives in quasi-isotropic turbulence. *Phys. Fluids* **12** (12) 3097–3099.

Gulitski, G., Kholmyansky, M., Kinzelbach, W., Lüthi, B., Tsinober, A. & Yorish, S. 2007 Velocity and temperature derivatives in high Reynolds number turbulent flows in the atmospheric surface layer. Part I. Facilities, methods and some general results. *J. Fluid Mech.* **589** 57–81.

Jeong, E. & Girimaji, S. S. 2003 Velocity-gradient dynamics in turbulence: effect of viscosity and forcing. *Theor. Comput. Fluid Dyn.* **16** 421–432.

Kholmyansky, M., Tsinober, A. & Yorish, S. 2001 Velocity derivatives in the atmospheric surface layer at Re-lambda=10^4. *Phys. Fluids* **13** (1) 311–314.

Li, Y., Perlman, E., Wan, M., Yang, Y., Burns, R., Meneveau, C., Burns, R., Chen, S., Szalay, A. & Eyink, G. 2008 A public turbulence database cluster and applications to study Lagrangian evolution of velocity increments in turbulence. *J. Turbul.* **9** (31) 1–29.

Lund, T. S. & Rogers, M. M. 1994 An improved measure of strain state probability in turbulent flows. *Phys. Fluids* **6** (5) 1838–1847.

Lüthi, B., Tsinober, A. & Kinzelbach, W. 2005 Lagrangian measurement of vorticity dynamics in turbulent flow. *J. Fluid Mech.* **528** 87–118.

Martín, J., Dopazo, C. & Valiño, L. 1998 Dynamics of velocity gradient invariants in turbulence: restricted Euler and linear diffusion models. *Phys. Fluids* **10** (8) 2012–2025.

Ooi, A., Martín, J., Soria, J. & Chong, M. 1999 A study of the evolution and characteristics of the invariants of the velocity-gradient tensor in isotropic turbulence. *J. Fluid Mech.* **381** 141–174.

Patterson, G. & Orszag, S. 1971 Spectral calculations of isotropic turbulence: efficient removal of aliasing interactions. *Phys. Fluids* **14** 2538–2514.

Soria, J., Sondergaard, R., Cantwell, B. J., Chong, M. S. & Perry, A. E. 1994 A study of the fine-scale motions of incompressible time-developing mixing layers. *Phys. Fluids* **6** (2) 871–884.

Sreenivasan, K. R. & Antonia, R. A. 1997 The phenomenology of small-scale turbulence. *Annu. Rev. Fluid Mech.* **29** 435–472.

Tennekes, H. & Lumley, J. L. 1972 *A First Course in Turbulence*. MIT Press.

Tsinober, A. 2001 *An Informal Introduction to Turbulence*. Kluwer Academic.

Tsinober, A., Ortenberg, M. & Shtilman, L. 1999 On depression of nonlinearity in turbulence. *Phys. Fluids* **11** 2291–2297.

Vieillefosse, P. 1982 Local interaction between vorticity and shear in a perfect incompressible fluid. *Le journal de Physique* **43** (6) 837–842.